Atmos. Chem. Phys. Discuss., 3, 3939–3989, 2003
www.atmos-chem-phys.org/acpd/3/3939/

Atmospheric Chemistry and Physics Discussions

Preindustrial-to-present-day radiative forcing by tropospheric ozone from improved simulations with the GISS chemistry-climate GCM

D. T. Shindell, G. Faluvegi, and N. Bell

NASA Goddard Institute for Space Studies, and Center for Climate Systems Research, Columbia University, New York, New York, USA

Received: 22 May 2003 – Accepted: 4 July 2003 – Published: 28 July 2003

Correspondence to: D. T. Shindell (dshindell@giss.nasa.gov)

Abstract

The tropospheric chemistry model used at the Goddard Institute for Space Studies (GISS) within the GISS general circulation model (GCM) to study interactions between chemistry and climate change has been expanded and integrated into a version of the GCM with higher vertical resolution. The chemistry now includes peroxyacetylnitrates and non-methane hydrocarbons in addition to background NO_x-HO_x-O_x-CO-CH_4 chemistry. The GCM has improved resolution and physics in the boundary layer, improved resolution near the tropopause, and contains a full representation of the stratosphere. Simulations of present-day conditions show that this coupled chemistry-climate model is better able to reproduce observed tropospheric ozone, especially in the tropopause region, which is critical to climate forcing. Comparison with simulations of preindustrial conditions gives a global annual average radiative forcing due to tropospheric ozone increases of 0.30 W/m^2 with standard assumptions for preindustrial emissions. Locally, the forcing reaches more than 0.8 W/m^2 in parts of the northern subtropics during spring and summer, and is more than 0.6 W/m^2 through nearly all the Northern subtropics and mid-latitudes during summer. An alternative preindustrial simulation with soil NO_x emissions reduced by two- thirds and emissions of isoprene, paraffins and alkenes from vegetation increased by 50% gives a forcing of 0.33 W/m^2. Given the large uncertainties in preindustrial ozone amounts, the true value may lie well outside this range.

1. Introduction

Changes in atmospheric chemistry since the industrial revolution have had a significant impact on climate and human health, but are difficult to quantify accurately due to their complexity [Intergovernmental Panel on Climate Change (hereafter IPCC), 2001]. Increased anthropogenic emissions of greenhouse gases and ozone precursor gases such as nitrogen oxides (NO_x) produce tropospheric ozone, a potent greenhouse gas,

ACPD

3, 3939–3989, 2003

and also alter the oxidation capacity of the troposphere. The latter change affects the lifetime of many trace gases, including methane, another powerful greenhouse gas. Tropospheric ozone changes have a spatial pattern that is extremely inhomogeneous, leading to similar inhomogenaity in its radiative forcing. We therefore feel it is useful to explore these chemical changes in a model in which they can be directly coupled to the concurrent climate changes during the past and those projected for the future.

The magnitude of the radiative forcing due to tropospheric ozone increases is relatively uncertain. This uncertainty arises from the paucity of observations during the preindustrial period, and the poor quality of those that do exist. Estimates are therefore based on model simulations, though these are subject to large uncertainties in emissions of ozone precursors in both modern and especially in preindustrial times. Though the IPCC presents estimates of the forcing from tropospheric ozone since the preindustrial of $+0.35 \pm 0.15$ W/m^2, several recent studies have indicated that the value may actually be significantly larger. These studies are based upon preindustrial emissions of precursors adjusted within their uncertainties to give a better match to the purported 19th century observations of surface ozone (Mickley et al., 2001), or estimates constrained by 20th century observations prior to the late 1970s onset of large amounts of stratospheric ozone depletion by chlorofluorocarbons (Shindell and Faluvegi, 2002). Both studies find that forcings of around 0.7 W/m^2 are reasonable.

Radiative forcing from tropospheric ozone is especially large (per unit ozone change) near the tropopause (Hansen et al., 1997). Estimates of ozone change in this region are therefore especially important for evaluating ozone's forcing. Ozone in this region is extremely sensitive to stratosphere-troposphere exchange and to production of NO_x by lightning (Grewe et al., 2001). Both these factors are only weakly constrained by present-day observations, and are largely unconstrained for the preindustrial era. It is therefore a priority that the chemistry-climate models used to estimate tropospheric ozone's radiative forcing provide accurate simulations in this region.

We have previously developed and evaluated a simplified tropospheric chemistry package within the GISS GCM and used that model to explore the preindustrial to

ACPD
3, 3939–3989, 2003

present-day radiative forcing from tropospheric ozone (Shindell et al., 2001). That model has also been applied to study the relative importance of individual emission changes and climate responses since the preindustrial (Grenfell et al., 2001), for the future (Grenfell et al., 2003), to an investigation of the origin and variability of upper tropospheric nitrogen oxides and ozone (Grewe et al., 2001), and to a study of dynamical-chemical coupling across the tropopause (Grewe et al., 2002). Comparison with observations for that model showed that it was able to simulate tropospheric ozone and related species reasonably well. However, with only 9 vertical layers, that model had very coarse resolution in the vicinity of the tropopause and a poor representation of the stratosphere, so that its primary deficiency was in simulating stratosphere-troposphere exchange and tropopause region ozone accurately. We present here a new version of the GISS coupled chemistry-climate model with greater vertical resolution and a full representation of the stratosphere. Given the resulting large increase in the computational expense of the climate model portion of the simulation, it was relatively inexpensive to add to the chemistry. We have therefore expanded the original simple HO_x-NO_x-O_x-CO-CH_4 chemistry to include isoprene and the peroxyacetylnitrate (PAN), alkene, alkyl nitrate, paraffin and aldehyde families. This new model has been used to simulate present-day conditions, and has been extensively compared with observations. We have then performed preindustrial simulations, and investigated the resulting radiative forcing.

2. Model description

2.1. Chemistry

The model includes the basic HO_x-NO_x-O_x-CO-CH_4 chemistry (HO_x = OH + HO_2; NO_x = NO + NO_2 + NO_3 + HONO; O_x = O + $O(^1D)$ + O_3) described in Shindell et al. (2001), as well as the additional molecules and chemical reactions shown in Tables 1 and 2. We make use of the "chemical family" approach, whereby reactions between

ACPD
3, 3939–3989, 2003

family members are assumed to be rapid enough to maintain steady-state (at night, however, NO_x changes are explicitly calculated). This allows a larger chemical time step and transport of the entire family as a single tracer. We also use "lumped families" for hydrocarbons and PANs, which is necessary for the model to run sufficiently rapidly to be useful for climate studies. Chemical reactions involving these gases are based on the similarity between the molecular bond structures within each family using the reduced chemical mechanism called the Carbon Bond Mechanism 4 (Gery et al., 1989; Houweling et al., 1998). This scheme has been validated extensively against smog chamber experiments and more detailed chemical schemes (Gery et al., 1988; Derwent, 1990; Paulson and Seinfeld, 1992; Tonnesen and Jeffries, 1994). Standard gas phase chemical reaction rates have been updated to recent values (Sander et al., 2000).

The chemical family approach of grouping radical species together, along with combining hydrocarbons with similar characteristics into lumped families, permits calculations requiring the transport of only sixteen species in the GCM (Table 1). After combining the short-lived radicals into equilibrated families, we find that all the species have long enough lifetimes that we can use an extremely simple explicit scheme to calculate chemical changes (except for HO_x, CH_3O_2, and C_2O_3, whose very short lifetimes keep them in equilibrium at all times). Calculations are performed using a chemical time step of 1 h.

The chemical scheme includes 77 reactions, 25 of which have been added to the previous scheme to account for reactions of PANs and NMHCs (Table 2). As with the simpler scheme, heterogeneous hydrolysis of N_2O_5 into HNO_3 takes place on sulfate aerosols, using the reaction rate coefficients given by Dentener and Crutzen (1993). Sulfate surface areas are taken from an online calculation performed with the 9-layer version of the GISS GCM (Koch et al., 1999), assuming a monodispersed size distribution. Photolysis rates are calculated every two hours using the Fast-J scheme (Wild et al., 2000). Phase transformations of soluble species are calculated based on the GCM's internal cloud scheme. We include transport within convective plumes,

ACPD
3, 3939–3989, 2003

scavenging within and below updrafts, rainout within both convective and large-scale clouds, washout below precipitating regions, evaporation of falling precipitation, and both detrainment and evaporation from convective plumes (Koch et al., 1999; Shindell et al., 2001). Dry deposition is based on a resistance-in-series calculation and prescribed (i.e. uncoupled) vegetation as described in Shindell et al. (2001). Chemical calculations are performed only in the troposphere in this version of the model, while stratospheric values of ozone, nitrogen oxides, and methane are prescribed according to satellite observations with seasonally varying abundances as in the standard GISS model (Hansen et al., 1996).

The model also includes a full representation of the global methane cycle, including the chemical oxidation chain and detailed emissions and sinks. Though not crucial for the simulations described here, calculation of methane as an active chemical constituent will allow for future investigations of interactions between climate change and methane emissions and oxidation. Note that water vapor is also an active chemical tracer in this model, in contrast to most chemical models which lack a detailed hydrological cycle, and can thus respond to changes in climate via surface temperatures and altered circulation patterns.

2.2. Sources and sinks

Emissions of NO_x and CO are largely unchanged from our previous model, based largely on the Global Emissions Inventory Activity (GEIA) data sets (Benkovitz et al., 1996; Olivier et al., 1996) and on Wang et al. (1998a). Total emissions of CO are 987.7 Tg/yr (490.1 from biomass burning and 497.6 from industrial activities). Prescribed emissions of NO_x were 20.9 Tg/yr N from fossil fuels, 5.8 from soils, 5.8 from biomass burning, and 0.6 from aircraft. We have added emissions of isoprene based on Wang et al. (1998a), and alkenes and paraffins also based on GEIA. Global annual average emissions of isoprene were scaled to 200 Tg/yr from vegetation, as in recent model intercomparisons (IPCC, 2001). Global annual average emissions of alkenes are 32.9 Tg/yr, made up of 16.0 Tg/yr from vegetation, 11.6 Tg/yr from industry, and 5.3 Tg/yr

ACPD
3, 3939–3989, 2003

from biomass burning. The largest single contributor is propene, which makes up nearly half the emissions for this family, with other alkenes and alkynes also contributing. Global annual average emissions of paraffins are 87.0 Tg/yr, made up of 14.0 Tg/yr from vegetation, 68.8 Tg/yr from industry, and 4.2 Tg/yr from biomass burning. For the industrial component, butane, pentane and higher alkanes are the largest sources, with smaller contributions from ethane and propane. The biomass burning component is dominated by ethane emissions. For both the alkene and paraffin families, the spatial and temporal distribution of isoprene emissions was used for vegetation, and that of carbon monoxide for biomass burning, for lack of further information, with the overall source value scaled to the emissions given above. Distributions of industrial emissions of alkenes and paraffins are from GEIA.

Methane emissions were based upon the data sets of Fung et al. (1991) (available at http://www.giss.nasa.gov/data/ch4fung). These fields were scaled to values within recent estimates of individual source strengths and their uncertainties (World Meteorological Organization (hereafter WMO), 1999), but maintaining the spatial distributions of the original data sets. The only exception was wetland emissions, which were shifted in latitude towards the tropics (x 1/3 poleward of 30° in both hemispheres, x 10/4 from 30° S–30° N) to match more recent estimates of their meridional distribution (WMO, 1995), and increased in magnitude to be more in line with recent estimates (Hein et al., 1997; Walter et al., 2001). Total emissions are 464.0 Tg/yr, made up of emissions from the following individual sources (in Tg/yr): animals (enteric fermentation in ruminants plus animal waste) 83.9, coal mining 20.1, pipeline leakage of natural gas 24.8, venting of natural gas at wells 17.0, landfills (including municipal solid waste) 27.5, termites 20.0, coal burning 16.0, ocean (including 3.0 from hydrates) 13.0, fresh water 5.0, miscellaneous ground sources (volcanoes and hydrothermal vents) 7.0, biomass burning 30.0, rice cultivation 30.0, wetlands and tundra 209.7. Loss of methane via absorption into soils is also included, with a value of −39.9 Tg/yr (Fung et al., 1991; WMO, 1994). Biomass burning, rice cultivation and wetlands/tundra include seasonal emission cycles.

ACPD
3, 3939–3989, 2003

As in the older model, the GISS convection scheme is used to derive both the total lightning and the cloud-to-ground lightning frequencies interactively in each grid box and at each time step (Price et al., 1997). Then the generation of NO_x from lightning is used to derive the NO_x produced, including a C-shaped vertical distribution (Pickering et al., 1998).

2.3. Climate model

The climate model used here is a version of the GISS model II' (two-prime) enhanced over that used previously with updated planetary boundary layer and convection schemes. Briefly, the GCM's boundary layer employs a finite modified Ekman layer with parameterizations for drag and mixing coefficients based on similarity theory, convection includes entraining and nonentraining plumes, mass fluxes proportional to convective instability, explicit downdrafts, and a cloud liquid water scheme, based on microphysical sources and sinks of cloud water, which carries both water and ice (Del Genio et al., 1996). The land surface parameterization calculates transpiration, infiltration, soil water flow and runoff, all of which impact both water vapor and latent heat release to the atmosphere. Chemical tracers, along with heat and moisture, are advected using a quadratic upstream scheme (Prather, 1986). Momentum advection uses a fourth-order scheme. The model's interhemispheric exchange times are within 15–25% of observations. Within the GISS chemistry modeling group we have focused on improving those aspects of the circulation that we believed would be most crucial for correctly simulating stratosphere-troposphere exchange. The gravity-wave drag scheme in this model version has been tested extensively and is now able to reproduce observed wind and temperature climatologies much better than in previous versions. This has led to notably improved transport of ozone down from the stratosphere, for example, which was heavily biased towards high latitudes and had an incorrect seasonal cycle in other model versions.

All simulations with the new chemistry have been performed using a version with $4 \times 5^{\circ}$ horizontal resolution and 23 vertical layers (Fig. 1). Note that the vertical

ACPD
3, 3939–3989, 2003

resolution has been significantly improved in both the boundary layer and near the tropopause, both regions crucial to ozone simulations, in addition to adding layers in the stratosphere (Fig. 1). The bottom 11 layers of this model are terrain-following levels, while the top 12 are constant pressure surfaces. The model time-step is one hour for both the chemistry and physics. Ozone calculated by the chemical model is coupled to the GCM's radiation calculation, so that chemical changes are able to affect meteorology. Monthly mean sea-surface temperatures and sea ice cover are prescribed to 1990–1999 average values (N. A. Rayner et al., Globally complete analyses of SST, sea ice, and night marine air temperature, 1871–2000, manuscript in preparation, 2003; hereafter Rayner_SST_2003) in these simulations for computational savings. Therefore the climate is not fully responsive to the chemistry. The importance of such coupling will be investigated in future simulations. All results presented here are averages over the last five years of seven year simulations. The model reaches equilibrium within the first year, and the interannual variability is relatively small compared to features of interest, so that five years gives us adequate statistics for mean values. The model has been run for present-day (1990) and for preindustrial (~1850) conditions. Additionally, a run with the older chemistry package lacking PANs and hydrocarbons higher than methane has been performed with the 23-layer GCM. This helps isolate the influence of the increased vertical resolution from the effect of the more sophisticated chemistry.

The more comprehensive chemistry scheme adds only about 24% to the running time of the GCM, plus an additional ~15% for the transport of the chemical tracers, for a total increase of only ~40%. It is therefore computationally rapid enough that the GCM can be run with online chemistry for long-term climate simulations or for multiple runs to examine the sensitivity of the results to various changes. Though the fractional time used for chemistry is less for the more complex chemistry in the 23-layer model than for the simplified chemistry in the 9-layer model (~40% versus ~55%), this is only because the physics takes much longer in the 23-layer version, where the calculations are both more sophisticated and done on more vertical levels. The absolute time taken

ACPD
3, 3939–3989, 2003

by the more complex chemistry is roughly a factor of 3 greater than for the simplified chemistry, both due to the increase in the number of reactions and tracers and to the increase of nearly a factor of two in the number of vertical levels within the troposphere.

3. Evaluation of present-day simulation

3.1. Ozone

We have compared modeled annual cycles of ozone with the ozonesonde climatology of Logan (1999). Comparisons at stations representative of a wide range of latitudes are shown in Fig. 2. Results from the earlier 9-layer model with simplified chemistry are also shown (for these comparisons, we have interpolated between model levels to the exact pressure levels of the sonde data, leading to slight differences as compared with the results shown for the older model in Shindell et al. (2001)). The new model clearly does a better job at matching the observations than the older model at the levels nearest the tropopause (125 and 200 hPa). This holds for both the tropics, where the ozone is primarily of tropospheric origin, and for middle and high latitudes, where for at least part of the year the air is primarily of stratospheric origin. At 200 hPa, a positive bias in the tropics in the 9-layer model has been eliminated. Comparison of the results from the 23-layer simulations using simplified chemistry against those with the more advanced scheme show that the improvement in this region results primarily from an improved representation of tropical upwelling rather than from chemistry. The model has difficulty reproducing the spring maximum in ozone at 200 hPa at Northern middle and high latitudes, though it does this fairly well in the Southern Hemisphere. This maximum is stratospheric air, and thus may indicate biases in the stratospheric ozone climatology. It should be noted, however, that the vertical gradient of ozone is extremely large at these altitudes, so that small differences in height can lead to ozone changes of hundreds of ppbv (this is true at 125 hPa as well). It may be that a near-perfect match with sondes can therefore only be obtained with extremely high vertical resolution in

ACPD
3, 3939–3989, 2003

this area. For those locations and seasons dominated by tropospheric air (i.e. with ozone values less than about 150 ppbv, such as Hohenpeissenberg during September and October and Lauder during January to April), the model does an excellent job of reproducing observed values. Results are fairly similar in the middle troposphere between the old and new models, though the positive bias at high latitudes is somewhat worse in the new version. Fortunately, these locations are less important for radiative forcing. At the surface most locations show small improvements, while the comparison with Hohenpeissenberg measurements is greatly improved. We attribute this largely to improvements in the boundary layer scheme of the GCM, including the higher vertical resolution there which allow more realistic dry deposition. Similar improvements in surface ozone values were seen at Pretoria and Sapporo (not shown).

We compare the ability of the two model versions to reproduce the observations over all the sites recommended for testing models by Logan et al. (1999) in Table 3. As noted, the quality of the new model's ozone simulation has improved markedly in the vicinity of the tropopause and near the surface. Biases in the vicinity of the tropopause are now very small. Though the 125 hPa level is often in the stratosphere, and thus merely reflects the climatology, improvements in the tropics, where this level is in the troposphere have reduced the bias there from 5% to 3% comparing the new model to the older version. At 200 hPa, the bias has been greatly reduced, from 23% to 12%. A similar level of improvement has been obtained at low levels, where biases have dropped to 11% and 8% at 500 and 950 hPa, respectively, from 16 and 31% in the older model. Similar improvements are apparent when examining the average absolute differences. In the middle troposphere, however, the average absolute difference between the model and the observations has increased. Evaluation of the average bias reveals that this results largely from a consistent positive bias in this region, much of which comes from the two high-latitude sites (Table 3). This likely results from deficiencies in the GCM's downward transport of stratospheric air at high latitudes, which also seems to affect the 500 hPa level at high latitudes. The positive bias at 300 hPa may also be related to the lightning NO_x production, which may be on the high side though

ACPD
3, 3939–3989, 2003

it is well within current uncertainty (see below, and note that reduced lightning NO_x would worsen the negative bias at 200 hPa). Except for the 300 hPa level, however, the systematic bias averaged over all 16 sites is roughly 10% or less. The average absolute difference between the model and the measurements is well within the observed standard deviation at all levels.

In general, the model does a good job of reproducing both the magnitude and seasonality of tropospheric ozone. While comparison between the 23-layer runs with simplified and advanced chemistry shows few obvious areas of improvement in the ozone fields, we nevertheless believe that incorporation of the advanced chemistry allows better simulation of tropospheric ozone in remote regions (where little validation data is available) and of ozone changes as a function of time, as well as doing a better job with other trace gases.

Surface ozone is shown in Fig. 3. Observations are well reproduced over most regions in this model. The model's surface level ozone over the remote North Atlantic during January is slightly greater than observations, 35–45 ppbv as compared with measurements showing values of 30–40 ppbv (Parrish et al., 1998). The observational data however include only 4 years of measurements from Sable Island (44° N, 60° W) and a single year from the Azores (39° N, 28° W), so should be treated with some caution. The addition of PANs has increased the amount of ozone in remote regions of the Northern Hemisphere, accounting for the increase here relative to the older model. In remote regions of the Southern Hemisphere, the model does an excellent job of reproducing the observed values. The model finds July values of 25–35 ppbv at Syowa station, a location where most models underpredict ozone (Shindell et al., 2001). Over the Southern Hemisphere continents, surface ozone has decreased significantly compared with the previous model version. For example, surface ozone over South America has dropped from 30–45 ppbv in the previous version to only 5–2 ppbv in the current model. The very low values seen in the new model during summer, 5–15 ppbv over the Amazon basin and 10–20 over the Brazilian savannah, are in agreement with measurements taken during the ABLE-2A summer campaign which showed near-surface

ACPD
3, 3939–3989, 2003

ozone values of about 8–16 ppbv over the Amazon and slightly larger values over the savannah (Kirchoff, 1988; Emmons et al., 2000). We attribute this change to the increase in hydrocarbons, which in regions with relatively low abundances of NO_x lead to ozone destruction. Values over the Southern Hemisphere oceans are quite similar in the two models, supporting a terrestrial influence.

The ozone budget in the new model is substantially altered from the previous version. However, we caution that this may not be a very useful indicator of the veracity of ozone simulations. As discussed in Shindell et al. (2001), models report widely differing budget values, yet all profess to simulate observed ozone amounts reasonably well. Furthermore, in testing the gravity-wave drag parameterization in the GCM, we discovered that changes in the stratosphere-troposphere exchange by a factor of two are largely compensated for by adjustment of the chemical and dry deposition terms to yield almost the same ozone fields in most areas. Another example comes from comparing the 9-layer simulation with the simplified chemistry to the 23-layer model with the same chemistry. Going to the higher resolution model reduced the stratosphere-troposphere exchange by 364 Tg/yr. In compensation for the reduced influx, the net tropospheric chemical production increased by 378 Tg/yr, leading to a relatively small increase in the ozone burden. Similarly, comparing the simulations of the 23-layer GCM using the previous, simplified chemistry and the present more complex scheme showed that the addition of higher hydrocarbon families and PANs caused an increase in the net chemical production of ozone of 201 Tg/yr. With a similar stratosphere-troposphere exchange in these two runs, the dry deposition increased by 191 Tg/yr, largely balancing the chemical changes and leading to an increase of only 18 Tg in the tropospheric ozone burden. Thus the system appears to be highly buffered, and changes to a given factor in ozone's budget often have little net effect. In the new model, the tropospheric ozone budget in terms of annual average fluxes (Tg/yr) is +417 stratosphere-troposphere exchange, −1466 dry deposition, and +1049 chemistry. The resulting ozone burden is 349 Tg. For comparison, the budget of the previous version was +750 stratosphere-troposphere exchange, − 1140 dry deposition, +389 chemistry,

ACPD
3, 3939–3989, 2003

and an ozone burden of 262 Tg. The values for dry deposition and chemistry found here are quite large, at the high end or outside the range reported for other models. Yet the tropospheric ozone burden is in good agreement with the 236-364 Tg range reported by other models (Roelofs and Lelieveld, 1995; Levy et al., 1997; Roelofs et al., 1997; Houweling et al., 1998; Wang et al., 1998b; Hauglustaine et al., 1998; Mickley et al., 1999; Stevenson et al., 2000; Lelieveld and Dentener, 2000).

The stratosphere-troposphere exchange was calculated using the flux across the 150 hPa surface for both the 9- and 23-layer models. Given the large gradients in the tropopause region, the precise value of the exchange is sensitive to the specific definition chosen. If instead we use the flux across the 250 or 75 hPa surfaces, we find values of 539 or 383 Tg/yr, respectively, in the new model. If we sum the horizontal and vertical fluxes across a surface at 300 hPa poleward of 30° and at 100 hPa in the tropics, we find a total net flux of 342 Tg/yr. Consistent with this range, the net chemistry term over the varyingly defined troposphere ranges from 1142 to 927 Tg/yr. The stratosphere-troposphere exchange term is the only one to have reasonably good constraints on its global value, which has been given a 450 Tg/yr best estimate with a 200–870 Tg/yr range for the cross-tropopause flux from ozone-NO_y tracer correlations (Murphy and Fahey, 1994), a value of 450–590 Tg/yr at 100 hPa based on satellite observations (Gettelman et al., 1997) and 390 Tg/yr at 150 hPa (Mickley et al., 1999) based on fluxes estimated from meteorological data (Appenzeller et al., 1996). Our comparable values are in the range of these estimates, and much better than that seen in our previous model.

If the dry deposition and chemistry were both very much too large, we might expect that although the budget would not be greatly affected since these terms oppose one another, there would be a systematic bias toward underprediction of ozone at low levels and overprediction elsewhere. The comparison with sondes (Fig. 2 and Table 2) does not support such a bias. In fact, the improvement in simulated surface ozone in polluted areas is largely attributable to the new planetary boundary layer scheme's enhancement of dry deposition. Based on the observational constraint of the lowest level

ACPD
3, 3939–3989, 2003

sonde data it appears that the faster dry deposition is more reasonable. We therefore believe that the budget is not a very useful constraint, aside from the stratosphere-troposphere exchange term, and that the key test is that we have demonstrated that the model does a reasonably good job of simulating observed ozone values.

3.2. Carbon monoxide

A comparison between observed and simulated annual cycles of surface carbon monoxide at several locations is shown in Fig. 4. The model does a good job of matching the measured values, though there are slight positive and negative biases at Cape Mears and Samoa, respectively. Compared with the simpler chemistry, this version does a better job of reproducing the observed seasonal cycle, which matches the observations quite well at all locations. The model has a global mean mass-weighted OH abundance of 9.7×10^5 molecules/cm^3 for the present day, matching the value of $9.4 \pm 1.3 \times 10^5$ molecules/cm^3 derived from measurements of the lifetime of the solvent methyl chloroform (Prinn et al., 2001). The ability of the model to reproduce the mean and seasonal cycle of CO so well implies that the seasonality and amount of hydroxyl is well-simulated. Note that we have chosen to use a much reduced isoprene source in order to improve the carbon monoxide and hydroxyl simulations, despite the lack of observational support for such a source strength, as in recent intercomparisons (IPCC, 2001). If we use the emission source inferred from observations, we find the typical positive bias in CO and negative bias in OH. It remains to be determined whether these biases result from deficiencies in current understanding of NMHC chemistry, in transport of emitted isoprene out of the canopy, or in some other factor.

3.3. Nitrogen species and lightning

The budget of nitrogen oxides is shown in Table 4. We compare measurements of NO_x and HNO_3 with modeled values in Fig. 5. Observations are not available with long-term coverage from a fixed location as they are with ozone, so we are forced to compare

ACPD
3, 3939–3989, 2003

with data obtained during brief field campaigns as compiled by Emmons et al. (2000). These may not be statistically representative, however. The sample of sites shown in the figure is representative of the behavior of many additional comparisons we performed. The model generally does a good job of reproducing observed profiles of NO_x. This is consistent with the model's ability to accurately simulate ozone. The model is generally capable of generating the very low values in the remote Pacific (Fig. 5). However, in a few regions, such as eastern Brazil (and southern Africa, not shown) the model cannot reproduce the very large values seen in the lower troposphere during the biomass burning period. Out over the South Atlantic the model gives a good match, but the continental values are too low, suggesting that at least during the year of the TRACE-A observations, biomass burning emissions of NO_x may have been larger than those in the GEIA inventory. Near highly polluted areas such as Japan, the model does an excellent job of matching the "C-shaped" profile found in observations (Fig. 5). In contrast to NO_x, the model's simulation of HNO_3 is often not in accord with observations in polluted regions. While the model mostly matches the observed profiles in the remote Pacific and over the Philippine Sea, it greatly overpredicts nitric acid amounts over eastern Brazil, Japan, and the South Atlantic (Fig. 5), as well as over many other locations near biomass burning regions or industrialized areas (not shown). The overprediction can be a factor of 5 or so, suggesting that the discrepancy is too large to be attributed simply to coarse model resolution or emission uncertainties. An overpredicition of nitric acid is a common problem in tropospheric chemistry models, and likely reflects a missing removal mechanism for nitric acid (since the NO_x values are reasonable). In the future, we intend to fully couple the chemistry in our model to the sulfate aerosol scheme, to consider the inclusion of ammonia chemistry, and to explore heterogeneous reactions on additional surface types such as mineral aerosols and ice which may address this problem.

The model's simulation of PANs is in fairly good agreement with observations in many locations (Fig. 6). PANs are underpredicted over Eastern Brazil during October, consistent with all the nitrogen species, and there is a suggestion of a systematic

ACPD
3, 3939–3989, 2003

overestimate in polluted regions. As with nitric acid, we are hopeful that improvement of the model's heterogeneous chemistry will address the latter problem. Additionally, our model uses a family of PANs, while the observations record only PAN itself, creating a systematic difference in the comparison.

The parameterized generation of NO_x from lightning produces 6.5 Tg/yr N in this model. This is significantly larger than the previous model's value of 3.9 Tg/yr, though within the expected range of 2–20 Tg/yr (WMO, 1999). The difference results from empirical adjustments made to the parameterization to better match observations, the altered convection scheme in the new model version, and the influence of the model's higher vertical resolution on the lightning NO_x parameterization. The spatial distribution of flashes is similar to that in the previous model, but is now in better agreement with Optical Transient Detector (OTD) satellite (Boccippio et al., 1998) observations (Fig. 7). The flash frequency averaged over all points is ~25% greater in the GCM than in the observations, though there are underestimates over the oceans off the eastern edge of continents and over Northern Hemisphere middle latitudes. The older model produced flash rates ~60–65% of those observed. This suggests that the new parameterization and convection scheme likely gives a somewhat more realistic overall NO_x production from lightning, though the current production may be positively biased.

3.4. Hydrogen peroxide and methyl hydroperoxide

The model does a generally good job reproducing observed hydrogen peroxide values in most regions regardless of season (Fig. 8). In contrast to the previous model version, the model is now able to capture the huge enhancement of H_2O_2 in the lower troposphere over Brazil in the fall, albeit with a somewhat reduced magnitude (as expected from the NO_x bias). The model's simulation over southern Africa during this time of year is also improved (not shown). The model exhibits a positive bias in the region of 900 hPa over portions of the Pacific similar to that shown for Fiji during March–April, but even larger at Tahiti, Hawaii, and Christmas Island. Given the overall high quality of the OH simulation, it seems likely that this is related to an underestimate of wet removal in

ACPD
3, 3939–3989, 2003

this region. It is also possible that the model's outflow of polluted air from Asia is too large, leading to too much chemical production of H_2O_2. Given the reasonably good quality of the simulated nitrogen oxides and nitric acid over the Pacific, however, this seems less likely.

The simulation of methyl hydroperoxide (CH_3OOH) is also quite good in this model (Fig. 9). The model's values are quite close to those observed for nearly all locations, including both highly polluted regions and the remote Pacific, and for all seasons. Accurate simulation of this important radical intermediate gives us confidence that the model's chemical oxidation of hydrocarbons is being calculated reliably.

3.5. Methane

The methane oxidation rate is 431 Tg/yr, consistent with the budget of methane given its large uncertainties. The interhemispheric gradient of methane is ~150 ppbv in these simulations (between averages over mid-to-high southern and northern latitude), in good agreement with 1990 observations (GLOBALVIEW-CH_4, 2001). This is not too surprising as the global OH values and the seasonal cycle of CO agree well with observations, implying that the oxidation is well modeled. We note that the model has more OH in the Northern Hemisphere than in the Southern, as in most models, but in contrast to the estimates of Prinn et al. (2001) (though those estimates have a very large uncertainty). Were the chemistry to produce an OH distribution matching those results, however, the interhemispheric gradient would grow larger. The seasonal cycle of methane appears exaggerated at high northern latitudes, however, though it is reasonable in the tropics and in the Southern Hemisphere. Future work will endeavor to improve the seasonality of our methane emissions datasets.

ACPD
3, 3939–3989, 2003

4. Preindustrial to present-day change

Many factors related to chemistry and climate have changed since the industrial revolution. A systematic study of the effect of each individual change with our previous model demonstrated that the reduced emissions of nitrogen oxides and methane dominated the overall forcing of tropospheric ozone change (Grenfell et al., 2001). To simulate preindustrial conditions, emissions of anthropogenic ozone precursors were eliminated (fossil fuels, industry and aircraft). Emissions from biomass burning were reduced to one-tenth of their present-day values, a common assumption also used in our earlier experiments. Sulfate surface areas were set to natural background levels as calculated by Koch et al. (1999). Monthly mean sea surface temperatures and sea ice conditions were prescribed according to reconstructed values from the 1870s (Rayner_SST_2003). The cooling relative to the present would be slightly larger for 1850 conditions, but this should have a minimal impact on the results (Grenfell et al., 2001). Concentrations of long-lived greenhouse gases were reduced as follows: CO_2 from 365 to 280 ppmv, N_2O from 314 to 275 ppbv, CH_4 from 1.745 to 0.700 ppmv, and CFCs to zero. Production of NO_x by lightning decreased to 6.2 Tg/yr in the preindustrial simulations, exhibiting a sensitivity to climate change in line with the +10% per degree of surface warming for this parameterization (Price and Rind, 1994).

Tropospheric ozone levels have increased markedly since the preindustrial (Fig. 10). Abundances have roughly doubled over much of the Northern Hemisphere from the equator to 45° N, with increases of more then 100% at low altitudes. The total tropospheric ozone burden has gone from 255 Tg to 349 Tg. This represents an increase of 37%, in accord with the 25–57% range reported in other models (Levy et al., 1997; Roelofs et al., 1997; Mickley et al., 1999; Lelieveld and Dentener, 2000) and similar to the 45% increase seen in our earlier simulations (Shindell et al., 2001). The tropospheric ozone budget for the preindustrial simulations is +449 Tg/yr from stratosphere-troposphere exchange, −829 Tg/yr from dry deposition, and +380 Tg/yr from chemistry. The strong dry deposition in this model draws down ozone so much that the net

chemical term is positive, in contrast to the previous version. Given that the net term is the difference between two very large production and destruction terms, this change is in fact not as large as it might appear. As with the present day simulations, we caution that the budget values may not provide a very useful measure of the ozone simulation. Overall, the pattern of ozone increase is fairly similar to that seen in other models and in our earlier simulations. However, the region of greatest increase (in ppbv) has shifted in comparison to our earlier simulations from about 80° N between ~600 and 80 hPa to 40° N from ~250 to 500 hPa. In percentage terms, the largest increase in both models takes place at Northern mid-latitudes near the surface. Increases of 80% now extend up to 250 hPa, while in the previous model version these went up to only ~500 hPa. The sensitivity above 500 hPa has likely been altered by the addition of non-methane hydrocarbons, which increased ozone production at upper levels, as seen in other models (e.g. Wang et al., 1998c). Enhanced lightning NO_x relative to the older model may have also contributed to the different response. The stratosphere-troposphere exchange was a greater contributor to tropospheric ozone in the preindustrial simulation than for the present day; 449 Tg/yr as compared to 417 Tg/yr. Analysis of the ozone fluxes reveals that this was primarily a result of the decreased upward flux of ozone from the troposphere at low latitudes, rather than a sizeable change in the downward flux from the stratosphere. Since the improved vertical resolution allowed a better simulation near the tropopause, and higher hydrocarbons are now included, the ozone changes simulated with the current model should be more trustworthy, especially in the upper troposphere. Occurring near the tropopause, they will certainly affect the radiative forcing, which we discuss further below.

The oxidation capacity of the troposphere has also changed since the preindustrial (Fig. 11). Near the surface in the Northern Hemisphere, the large increase in pollution in the present has caused a substantial increase in the abundance of OH, up to 50% in some locations. Hydroxyl production is increased by direct production via the $O(^1D)$ reaction with water, which is enhanced both by the global warming-induced increase in water vapor and the ozone pollution-induced increase in photolytic production of

ACPD
3, 3939–3989, 2003

$O(^1D)$. Furthermore, the increased hydrocarbons lead to HO_x production, though they also reduce the amount of OH by conversion to HO_2. In regions with less abundant NO_x, such as the Southern Hemisphere and the middle and upper troposphere in the Northern Hemisphere, the latter effect dominates, so that the amount of OH has decreased in those areas despite the increased ozone and water vapor. In the heavily polluted regions of the Northern Hemisphere, however, the hydrocarbon production of HO_x dominates, so that they further add to the overall increase in OH. The offsetting influences of the regions that show OH increases with those that show decreases leads to an overall OH reduction of 13.3% from the preindustrial to the present. Other models have reported responses ranging from 17% decreases to 6% increases (Brasseur et al., 1998; Mickley et al., 1999; Berntsen et al., 1997). The reduction in OH calculated here yields a comparable increase in the lifetime of methane.

5. Radiative forcing

The global mean annual average radiative forcing at the tropopause from the tropospheric ozone increase between the preindustrial and the present-day is 0.30 W/m^2 in these simulations (Fig. 12). The forcing is larger in the Northern Hemisphere, where its average value is 0.38 W/m^2, than in the Southern Hemisphere where its average values is only 0.22 W/m^2. Maximum forcings of 0.7 W/m^2 occur in the Northern subtropics, where the ozone changes also maximized and where sunlight is plentiful. The forcing drops below 0.1 W/m^2 only over Antarctica, where the ozone increases have been smallest and insolation is weakest. The spatial pattern of the forcing in this model looks quite similar to the results of other groups as shown, for example, in the IPCC report (2001). Seasonally, the greatest forcing is during July-August (and is nearly as large during March–May), when the forcing is larger than 0.6 W/m^2 over nearly the entire Northern Hemisphere subtropics and mid-latitudes, and surpasses 0.8 W/m^2 over parts of the subtropics (Fig. 13). The radiative forcing was calculated by calling the radiation code twice, once with the climatological ozone and once with the model's cal-

ACPD
3, 3939–3989, 2003

culated distribution. Then the change in this difference between the preindustrial and the present-day was calculated. Note that these results are not directly comparable to those presented for our previous model, which were for the top of the atmosphere rather than the tropopause. We believe the latter is a more useful diagnostic. The radiative forcing is primarily driven by absorption of longwave radiation (Fig. 14). Shortwave radiation plays the dominant role only at high latitudes, where the albedo is very high.

The global annual average forcing calculated here, 0.30 W/m^2, is in accord with the range of 0.28 - 0.55 W/m^2 reported by other three-dimensional global models (Hauglustaine et al., 1994; Roelofs et al., 1997; van Dorland et al., 1997; Berntsen et al., 1997; Stevenson et al., 1998; Haywood et al., 1998; Brasseur et al., 1998; Kiehl et al., 1999; Mickley et al., 1999; Lelieveld and Dentener, 2000). The uncertainty associated with this forcing is quite large, however, as the preindustrial sources are poorly constrained. To explore the range of potential preindustrial ozone levels, we performed an additional preindustrial run setting the soil NO_x emissions, much of which result from fertilizer application, to one-third their present-day value and increasing the emission of isoprene, paraffins and alkenes from vegetation by half to account for greater forested area in the past, following Mickley et al. (2001). In the "standard" preindustrial run, all of these emissions were kept unchanged from present-day values. The resulting global mean annual average radiative forcing from the present to the "alternative" preindustrial was 0.33 W/m^2, with a spatial distribution very similar to that seen in the "standard" case (Fig. 12).

A common test of preindustrial simulations is to compare with purported nineteenth century surface observations. We refer to these as "purported" observations due to their lack of quantitative reliability. Nearly all of these measurements were taken with a method known as the Schönbein technique, involving exposure of a chemically treated piece of paper to the air. Modern evaluations of this technique have shown that the results are highly dependent upon a variety of factors, such as the exposure time or the type of paper used, which were not controlled in the early observations (Kley et al., 1988; Pavelin et al., 1999). These results are thus useful primarily in a qualita-

ACPD
3, 3939–3989, 2003

tive sense. The only exceptions are the measurements from Montsouris, which were performed with a quantitative technique (Volz and Kley, 1988) (though even those data were affected by the influence of SO_2 and they may only reflect local conditions in the vicinity of Paris (Staehelin et al., 1994)). Though of limited quantitative use, we compare model results from the two preindustrial simulations with the nineteenth century purported observations (Fig. 15). The "alternative" simulation appears to do a slightly better job of matching the data points. As with other models (e.g. Mickley et al., 2001), there is little evidence of a seasonal cycle at Luanda and a mild positive bias remains at Montsouris. In any case, there is certainly no evidence to suggest that the larger ozone changes and radiative forcing associated with the "alternative" preindustrial run are too large.

6. Discussion and conclusions

We have developed an improved tropospheric chemistry model which has been coupled to a version of the GISS climate model with enhanced vertical resolution in the boundary layer, near the tropopause, and in the stratosphere. The new chemistry scheme now includes both peroxyacetylnitrates and non-methane hydrocarbons. Through the use of chemical families and a simple explicit chemical solver, the model's computational expense has been kept quite low. Nevertheless, the model does a reasonably good job of reproducing observed annual cycles and vertical profiles of ozone at many locations. The model's main bias is an overestimation of ozone in the middle troposphere at high-latitudes. This has a minimal effect on radiative forcing since insolation is weakest near the poles. The present model calculates a tropopause radiative forcing due to tropospheric ozone increases between the preindustrial and the present of 0.30 W/m^2. Given the increased resolution near the tropopause, a region of paramount importance for radiative forcing, and the improved chemistry, we believe the current results are more trustworthy than those of our earlier simulations.

Uncertainties in the preindustrial to present-day radiative forcing remain large, how-

ACPD
3, 3939–3989, 2003

ever, primarily due to the extremely poor constraints on preindustrial emissions of ozone precursors. We performed a test of altered assumptions for preindustrial emissions for comparison with the results of another chemistry model used with a simpler version of the GISS GCM (Mickley et al., 2001). The results of Mickley et al. (1999) showed a radiative forcing of 0.44 W/m^2 in their standard simulations. In our standard preindustrial case, soil NO_x emissions were unchanged from the present, while in the Mickley et al. (1999) simulations, soil NO_x emissions from fertilizer were removed. An additional difference between the models is that Mickley et al. (1999) used a larger biomass burning NO_x source, making the reduction to preindustrial times (based on a 90% decrease) also larger. However, an additional run of our new model using 7.7 Tg/yr N from biomass burning (van Aardenne et al., 2001) compared with the standard preindustrial run gave an identical forcing to our initial present-day simulation (using 5.3 Tg/yr N from biomass burning), suggesting that the forcing is not greatly sensitive to these emissions. Overall then, the emission differences are consistent with the larger radiative forcing found in Mickley et al's standard preindustrial to present-day case, though differences in the GCM versions used likely also contributed. Using altered assumptions for preindustrial emissions of soil NO_x, hydrocarbons from vegetation, and lightning, Mickley et al. (2001) found a radiative forcing of 0.72–0.80 W/m^2. They concluded that the increased forcing arose primarily from lightning, which they reduced by 43–71% (1.5-2.5 Tg N/yr). As our lightning change was only 5% (0.3 Tg N/yr), it is not surprising that our alternative simulation of the preindustrial showed less of an increase in the forcing. Given current uncertainties in the sensitivity of lightning to climate change, it remains unknown how large the change in that source really has been. Our sensitivity of lightning to climate may be on the low side, however, as a recent study suggests a sensitivity (lightning flash rate increase per degree of surface warming) of ~40%/K (Reeve and Toumi, 1999), as opposed to the ~10%/K sensitivity in the Price and Rind (1994) parameterization used here. Additionally, our preindustrial simulation was driven by sea-surface temperatures from the 1870s (the earliest in the data set), which neglects a small portion of the warming since the preindustrial, thus giving the

ACPD
3, 3939–3989, 2003

lightning less to respond to. Finally, these simulations did not account for any changes in stratospheric ozone, which could have affected both stratosphere-troposphere exchange and the flux of OH-forming ultraviolet radiation reaching the troposphere.

In addition to using models to estimate the preindustrial to present-day radiative forcing due to tropospheric ozone, another study has examined the earliest available ozone observations dating from the middle part of the twentieth century to evaluate long-term ozone trends (Shindell and Faluvegi, 2002). They concluded that the radiative forcing due to tropospheric ozone increases from the late 1950s to 2000 was 0.38± 0.10 W/m^2. Assuming even a very modest ozone buildup prior to 1950, the forcing since the preindustrial would then have been in the area of 0.5–0.6 W/m^2, on the high side of most global model simulations. Extrapolating based on the rate of increase of NO_x emissions (van Aardenne et al., 2001), the ozone precursor which is most often rate limiting, the radiative forcing would have been about 0.6 W/m^2 (Shindell and Faluvegi, 2002). Thus the radiative forcing from tropospheric ozone remains poorly constrained from both observations and models, but within the range of plausible values, it may have been one of the most important greenhouse gas forcings of modern climate change.

Acknowledgements. The authors thank NASA's Atmospheric Chemistry Modeling and Analysis Program for support, the Global Hydrology Resource Center at the Global Hydrology and Climate Center for supplying the archived OTD data, J. Logan and L. K. Emmons for kindly providing observational data, and Y. Hu for extensive testing and improvements to the GCM's gravity-wave parameterization.

References

Appenzeller, C., Holton, J. R., and Rosenlof, K. H.: Seasonal variation of mass transport across the tropopause, J. Geophys. Res., 101, 15 071–15 078, 1996.

Benkovitz, C. M., Scholtz, M. T., Pacyna, J., Tarrason, L., Dignon, J., Voldner, E. C., Spiro, P. A., Logan, J. A., and Graedel, T. E.: Global gridded inventories of anthropogenic emissions of sulfur and nitrogen, J. Geophys. Res., 101, 29 239–29 253, 1996.

Berntsen, T. K., Isaksen, I. S., Myhre, G., Fuglestvedt, J. S., Stordal, R., Larsen, T. A., Freckleton, R. S., and Shine, K. P.: Effects of anthropogenic emissions on tropospheric ozone and its radiative forcing, J. Geophys. Res., 102, 28 101–28 126, 1997.

Boccippio, D. J., Driscoll, K., Koshak, W., Blakeslee, R., Boeck, W., Mach, D., Christian, H. J., and Goodman, S. J.: Cross-sensor validation of the Optical Transient Detector (OTD), J. Atmos. Sol. Terr. Phys., 60, 701–712, 1998.

Brasseur, G. P., Kiehl, J. T., Müller, J. F., Schneider, T., Granier, C., Tie, X., and Hauglustaine, D.: Past and future changes in global tropospheric ozone: Impact on radiative forcing, Geophys. Res. Lett., 25, 3807–3810, 1998.

Del Genio, A., Yao, M.-S., Kovari, W., and Lo, K. K.-W.: A prognostic cloud water parameterization for global climate models, J. Clim., 9, 207–304, 1996.

Dentener, F. J. and Crutzen, P. J.: Reaction of N_2O_5 on tropospheric aerosols: Impact on the global distributions of NO_x, O_3 and OH, J. Geophys. Res., 98, 7149–7163, 1993.

Derwent, R. G.: Evaluation of a number of chemical mechanisms for their application in models describing the formation of photochemical ozone in Europe, Atmos. Env., 30, 2615–2624, 1990.

Emmons, L. K., Hauglustaine, D. A., Müller, J. F., Carroll, M. A., Brasseur, G. P., Brunner, D., Staehelin, J., Thouret, V., and Marenco, A.: Data composites of airborne observations of tropospheric ozone and its precursors, J. Geophys. Res., 105, 20 497–20 538, 2000.

Fung, I., John, J., Lerner, J., Matthews, E., Prather, M., Steele, L.P., and Fraser, P.J.: Three-dimensional model synthesis of the global methane cycle, J. Geophys. Res. 96, 13 033–13 065, 1991.

Gery, M. W., Whitten, G. Z., Killus, J. P., and Dodge, M. C.: Development and testing of the CBM-4 for urban and regional modelling, Rep. EPA-600/3-88-012, U. S. Environ. Prot. Agency, Research Triangle Park, NC, 1988.

Gery, M. W., Whitten, G. Z., Killus, J. P., and Dodge, M. C.: A photochemical kinetics mechanism for urban and regional scale computer modeling, J. Geophys. Res., 94, 925–956, 1989.

Gettelman, A., Holton, J. R., and Rosenlof, K. H.: Mass fluxes of O_3, CH_4, N_2O, and CF_2Cl_2 in the lower stratosphere calculated from observational data, J. Geophys. Res., 102, 19 149–19 159, 1997.

GLOBALVIEW-CH 4: Cooperative Atmospheric Data Integration Project – Methane. CD-ROM, NOAA CMDL, Boulder, Colorado [Also available on Internet via anonymous FTP to ftp.cmdl.noaa.gov, Path: ccg/ch4/GLOBALVIEW], 2001.

ACPD

3, 3939–3989, 2003

Grenfell, J. L., Shindell, D. T., Koch, D., and Rind, D.: Chemistry-climate interactions in the Goddard Institute for Space Studies general circulation model 2. New insights into modeling the preindustrial atmosphere, J. Geophys. Res., 106, 33 435–33 452, 2001.
Grenfell, J. L., Shindell, D. T., and Grewe, V.: Sensitivity studies of oxidative changes in the troposphere in 2100 using the GISS GCM, Atmos. Chem. Phys. Disc., 3, 1805–1842, 2003.
Grewe, V., Brunner, D., Dameris, M., Grenfell, J. L., Hein, R., Shindell, D., and Staehelin, J.: Origin and variability of upper tropospheric nitrogen oxides at northern midlatitudes, Atmos. Env., 35, 3421–3433, 2001.
Grewe, V., Reithmeier, C., and Shindell, D. T.: Dynamical-chemical coupling of the upper troposphere and lower stratosphere region, Chemosphere, 47, 851–861, 2002.
Hansen, J., Sato, M., Ruedy, R., et al.: A Pinatubo climate investigation, in The Effects of Mt. Pinatubo Eruption on the Atmosphere and Climate, NATO ASI Ser. Subser. 1, Global Environment Change, edited by G. Fiocco, D. Fua, and G. Visconti, 233–272, Springer-Verlag, New York, 1996.
Hansen, J., Sato, M., and Ruedy, R.: Radiative forcing and climate response, J. Geophys. Res., 102, 6831–6864, 1997.
Hauglustaine, D. A., Granier, C., Brasseur, G. P., and Megie, G.: The importance of atmospheric chemistry in the calculation of radiative forcing on the climate system, J. Geophys. Res., 99, 1173–1186, 1994.
Hauglustaine, D. A., Brasseur, G. P., Walters, S., Rasch, P. J., Müller, J. F., Emmons, L. K., and Carroll, M. A.: MOZART: A global chemical transport model for ozone and related chemical tracers, 2, Model results and evaluation, J. Geophys. Res., 103, 28 291–28 335, 1998.
Haywood, J. M., Schwarzkopf, M. D., and Ramaswamy, V.: Estimates of radiative forcing due to modeled increases in tropospheric ozone, J. Geophys. Res., 103, 16 999–17 007, 1998.
Hein, R., Crutzen, P. J., and Heimann, M.: An inverse modeling approach to investigate the global atmospheric methane cycle, Global Biogeochem. Cycles, 11, 43–76, 1997.
Houweling, S., Dentener, F., and Lelieveld, J.: The impact of non-methane hydrocarbon compounds on tropospheric photochemistry, J. Geophys. Res., 103, 10 673–10 696, 1998.
Intergovernmental Panel on Climate Change, Climate Change 2001. J. T. Houghton, et al. (eds). Cambridge University Press, Cambridge, England, 881 pp, 2001.
Kiehl, J. T., Schneider, T. L., Portmann, R. W., and Solomon, S.: Climate forcing due to tropospheric and stratospheric ozone, J. Geophys. Res., 104, 31 239–31 254, 1999.
Kirchhoff, V. W. J. H.: Surface ozone measurements in Amazonia, J. Geophys. Res., 93, 1469–

1476, 1988.
Kley, D., Volz, A., and Mulheims, F.: Ozone measurements in historic perspective, in Tropospheric Ozone, I. S. A. Isaksen (Ed.), D. Reidel Publishing Co., 63–78, 1988.
Koch, D., Jacob, D., Tegen, I., Rind, D., and Chin, M.: Tropospheric sulfur simulation and sulfate direct radiative forcing in the Goddard Institute for Space Studies general circulation model, J. Geophys. Res., 104, 23 799–23 822, 1999.
Lelieveld, J. and Dentener, F. J.: What controls tropospheric ozone?, J. Geophys. Res., 105, 3531–3551, 2000.
Levy, H. II, Kasibhatla, P. S., Moxim, W. J., Klonecki, A. A., Hirsch, A. I., Oltmans, S. J., and Chameides, W. L.: The global impact of human activity on tropospheric ozone, Geophys. Res. Lett., 24, 791–794, 1997.
Logan, J. A., An analysis of ozonesonde data for the troposphere: Recommendations for testing 3-D models and development of a gridded climatology for tropospheric ozone, J. Geophys. Res., 104, 16 115–16 149, 1999.
Mickley, L. J., Murti, P. P., Jacob, D. J., Logan, J. A., Koch, D. M., and Rind, D.: Radiative forcing from tropospheric ozone calculated with a unified chemistry climate model, J. Geophys. Res., 104, 30 153–30 172, 1999.
Mickley, L. J., Jacob, D. J., and Rind, D.: Uncertainty in preindustrial abundance of tropospheric ozone: Implications for radiative forcing calculations, J. Geophys. Res., 106, 3389–3399, 2001.
Murphy, D. M., and Fahey, D. W.: An estimate of the flux of stratospheric reactive nitrogen and ozone into the troposphere, J. Geophys. Res., 99, 5325-5332, 1994.
Olivier, J. G. J., Bouwman, A. F., Van der Maas, C. W. M., Berdowski, J. J. M., Veldt, C., Bloos, J. P. J., Visschedijk, A. J. H., Zandveld, P. Y. J., and Haverlag, J. L.: Description of EDGAR Version 2.0: A set of global emission inventories of greenhouse gases and ozone-depleting substances for all anthropogenic and most natural sources on a per country basis and on 1x1 grid. RIVM Techn. Report nr. 771060 002; TNO-MEP report nr. R96/119. National Institute of Public Health and the Environment, Bilthoven, December 1996.
Parrish, D. D., Trainer, M., Holloway, J. S., et al.: Relationships between ozone and carbon monoxide at surface sites in the North Atlantic region, J. Geophys. Res., 103, 13 357–13 376, 1998.
Paulson, S. E. and Seinfeld, J. H.: Development and evaluation of a photooxidation mechanism for isoprene, J. Geophys. Res., 97, 20 703–20 715, 1992.

ACPD
3, 3939–3989, 2003

Pavelin, E. G., Johnson, C. E., Rughooputh, S., and Toumi, R.: Evaluation of preindustrial surface ozone measurements made using the Schönbein method, Atmos. Environ., 33, 919–929, 1999.
Pickering, K. E., Wang, Y., Tao, W.-K., Price, C., and Müller, J.-F.: Vertical distributions of lightning NO_x for use in regional and global chemical transport models, J. Geophys. Res., 103, 31 203–31 216, 1998.
Prather, M.: Numerical advection by conservation of second-order moments, J. Geophys. Res., 91, 6671–6681, 1986.
Price, C., Penner, J., and Prather, M.: NO_x from lightning, 1, Global distribution based on lightning physics, J. Geophys. Res., 102, 5929–5941, 1997.
Price, C., and Rind, D.: Possible implications of global climate change on global lightning distributions and frequencies, J. Geophys. Res., 99, 10 823–10 831, 1994.
Prinn, R. G., Huang, J., Weiss, R. F., et al.: Evidence for substantial variations of atmospheric hydroxyl radicals in the past two decades, Science, 292, 1882–1888, 2001.
Reeve, N. and Toumi, R.: Lightning activity as an indicator of climate change, Q. J. R. Meteorol. Soc., 125, 893–903, 1999.
Roelofs, G.-J. and Lelieveld, J.: Distribution and budget of O_3 in the troposphere calculated with a chemistry general circulation model, J. Geophys. Res., 100, 20 983–20 998, 1995.
Roelofs, G.-J., Lelieveld, J., and Van Dorland, R.: A three-dimensional chemistry/general circulation model simulation of anthropogenically derived ozone in the troposphere and its radiative forcing, J. Geophys. Res., 102, 23 389–23 401, 1997.
Sander, S. P., Friedl, R. R., DeMore, W. B., et al.: Chemical kinetics and photochemical data for use in stratospheric modeling, Eval. 13, JPL Publ. 00-003, 2000.
Shindell, D. T., Grenfell, J. L., Rind, D., Price, C., and Grewe, V.: Chemistry climate interactions in the Goddard Institute for Space Studies general circulation model 1. Tropospheric chemistry model description and evaluation, J. Geophys. Res., 106, 8047–8076, 2001.
Shindell, D. T. and Faluvegi, G.: An exploration of ozone changes and their radiative forcing prior to the chlorofluorocarbon era, Atmos. Chem. Phys., 2, 363–374, 2002.
Staehelin, J., Thudium, J., Buehler, R., Volz-Thomas, A., and Graber, W.: Trends in surface ozone at Arosa (Switzerland), Atmos. Env., 28, 75–87, 1994.
Stevenson, D. S., Johnson, C. E., Collins, W. J., Derwent, R. G., Shine, K. P., and Edwards, J. M.: Evolution of tropospheric radiative forcing, Geophys. Res. Lett., 25, 3819–3822, 1998.
Stevenson, D. S., Johnson, C. E., Collins, W. J., and Derwent, R. G.: Future estimates of

ACPD
3, 3939–3989, 2003

tropospheric ozone radiative forcing and methane turnover – the impact of climate change, Geophys. Res. Lett., 27, 2073–2076, 2000.
Tonnesen, S. and Jeffries, H. E.: Inhibition of the odd oxygen production in the carbon bond four and generic reaction set mechanisms, Atmos. Environ., 28, 1339–1349, 1994.
van Aardenne, J. A., Dentener, F. J., Olivier, J. G. J., Klein Goldewijk, C. G. M., and Lelieveld, J.: A $1^{\circ} \times 1^{\circ}$ resolution data set of historical anthropogenic trace gas emissions for the period 1890-1990, Global Biogeochem. Cycles, 15, 909–928, 2001.
van Dorland, R., Dentener, F. J., and Lelieveld, J.: Radiative forcing due to tropospheric ozone and sulfate aerosol, J. Geophys. Res., 102, 28 079–28 100, 1997.
Volz, A. and Kley, D.: Evaluation of the Montsouris series of ozone measurements made in the nineteenth century, Nature, 332, 240–242, 1988.
Walter, B. P., Heimann, M., and Matthews, E.: Modeling modern methane emissions from natural wetlands 1. Model description and results, J. Geophys. Res., 106, 34 189–34 206, 2001.
Wang, Y., Jacob, D., and Logan, J.: Global simulation of tropospheric O_3–NO_x hydrocarbon chemistry, 1, Model formulation, J. Geophys. Res., 103, 10 713–10 725, 1998a.
Wang, Y., Jacob, D., and Logan, J.: Global simulation of tropospheric O_3–NO_x hydrocarbon chemistry, 2, Model evaluation and global ozone budget, J. Geophys. Res., 103, 10 727–10 755, 1998b.
Wang, Y., Jacob, D., and Logan, J.: Global simulation of tropospheric O_3–NO_x hydrocarbon chemistry, 3, Origin of tropospheric ozone and effects of nonmethane hydrocarbons, J. Geophys. Res., 103, 10 757–10 767, 1998c.
Wild, O., Zhu, X., and Prather, M. J.: Fast-J: Accurate simulation of in- and below-cloud photolysis in tropospheric chemical models, J. Atmos. Chem., 37, 245–282, 2000.
World Meteorological Organization, Scientific assessment of ozone depletion: 1994, Rep. 37, Geneva, 1995.
World Meteorological Organization, Scientific assessment of ozone depletion: 1998, Rep. 44, Geneva, 1999.

ACPD
3, 3939–3989, 2003

Table 1. Gases included in the model

Transported		Not transported	
(1)	O_x	(17)	NO
(2)	NO_x	(18)	NO_2
(3)	HNO_3	(19)	NO_3
(4)	N_2O_5	(20)	HONO
(5)	HO_2NO_2	(21)	OH
(6)	H_2O_2	(22)	HO_2
(7)	CO	(23)	O
(8)	HCHO	(24)	$O(^1D)$
(9)	CH_3OOH	(25)	O_3
(10)	H_2O	(26)	CH_3O_2
(11)	CH_4 [b]	(27)	**C_2O_3**
(12)	**PANs** [c]	(28)	**Aldehydes** [d]
(13)	**Isoprene**	(29)	**XO_2** [e]
(14)	**Alkyl Nitrates** [d]	(30)	**XO_2N** [f]
(15)	**Alkenes** [d]	(31)	**RXPAR** [g]
(16)	**Paraffins** [d]	(32)	**ROR** [h]

[a] Additional gases in the more comprehensive chemistry scheme are in bold face type.
[b] Transport of methane is optional.
[c] PANs are peroxyacetylnitrate and higher PANs.
[d] Alkyl Nitrates, Alkenes, Paraffins, and Aldehydes are lumped families. Alkenes includes propene, >C3 alkenes, and >C2 alkynes, Paraffins include ethane, propane, butane, pentane, >C5 alkanes and ketones, while Aldehydes include acetaldehyde and higher aldehydes (not formaldehyde).
[e] XO_2 is an NO to NO_2 operator.
[f] XO_2N is an NO to alkyl nitrates operator.
[g] RXPAR is a Paraffin budget corrector.
[h] ROR are radical byproducts of Paraffin oxidation.

ACPD
3, 3939–3989, 2003

Table 2. Additional reactions included in the model

	Bimolecular Reactions					A Factor	Activation Temperature
(1)	PAN → C_2O_3 + NO_2					2.00E+16	13500.
(2)	Isoprene + OH → .61HCHO + .58Alkenes + .85XO_2 + .85HO_2 + .15XO_2N + .63Paraffin					2.54E-11	-410.
(3)	Isoprene + O_3 → .9HCHO + .55Alkenes + .36CO + .15C_2O_3 + .63Paraffin + .30HO_2 + .18XO_2 + .28OH					1.23E-14	2013.
(4)	Isoprene + NO_3 → .9HO_2 + .45Alkenes + .9Alkyl Nitrates + .12Aldehydes + .1NO_2 + .03HCHO					7.80E-13	0.
(5)	Alkyl Nitrates + OH → NO_2 + XO_2					1.78E-12	0.
(6)	Alkenes + OH → HCHO + Aldehydes + XO_2 + HO_2 + RXPAR					5.20E-12	0.
(7)	Alkenes + O_3 → .64HCHO + .37CO + .44Aldehydes + .25HO_2 + .29XO_2 + .9RXPAR + .4OH					4.33E-15	1800.
(8)	Alkenes + NO_3 → HCHO + NO_2 + .91XO_2 + .09XO_2N + Aldehydes + RXPAR					7.70E-15	0.
(9)	Paraffin + OH → .11HO_2 + .87XO_2 + .76ROR + .11Aldehydes + .11RXPAR +.13XO_2N					8.10E-13	0.
(10)	Aldehyde + OH → C_2O_3					7.00E-12	-250.
(11)	Aldehyde + NO_3 → C_2O_3 + HNO_3					2.50E-15	0.
(12)	C_2O_3 + NO → HCHO + NO_2 + HO_2 + XO_2					3.50E-11	180.
(13)	C_2O_3 + C_2O_3 → 2HCHO + 2XO_2 + 2HO_2					2.00E-12	0.
(14)	C_2O_3 + HO_2 → HCHO + XO_2 + HO_2 + .79OH +CH_3OOH					6.50E-12	0.
(15)	ROR → 1.1Aldehyde + .94HO_2 + .96XO_2 + .04XO_2N + .02ROR +2.1RXPAR					1.00E+15	8000.
(16)	ROR → HO_2					1.60E+03	0.
(17)	XO_2 + HO_2 → CH_3OOH					3.50E-13	-1000.
(18)	XO_2 + NO → NO_2					4.20E-12	-180.
(19)	XO_2 + XO_2 →					1.70E-14	-1300.
(20)	XO_2N + NO → Alkyl Nitrates					6.80E-13	0.
(21)	XO_2N + HO_2 → CH_3OOH					(R17x R20)/R18	
(22)	RXPAR + Paraffin →					8.00E-11	0.
	Termolecular Reactions	k_o		n	k_∞		m
(23)	C_2O_3 + NO_2 → PAN	2.60E-28		7.1	1.20E-11		0.9
	Photolysis Reactions						
(24)	PAN + hv → C_2O_3 + NO_2						
(25)	Aldehyde + hv → HCHO + CO						

Reaction rates for bimolecular reactions are given by A exp ((-E/R)(1/T), where A is the Arrhenius A factor, E/R is the activation temperature of the reaction, and T is the temperature. For termolecular reactions, rates are calculated as a function of the high- and low-pressure reactions rates, given by $k\infty$(T/300)-m and ko(T/300)-n, respectively, where T is temperature. In all the above reactions, M is any body that can serve to carry away excess energy. For reaction 21, the rate is calculated based on the reaction rates of other reactions, as indicated. All rate coefficients taken from Houweling et al. (1998). Read 2.00E+16 as 2.00 x 10^{+16}.

ACPD

3, 3939–3989, 2003

Table 3. Ozone differences (ppbv) between models and sondes

Pressure level (hPa)	Average difference 9-layer model, all sites	Average difference, 23-layer model, all sites	Average bias, 9-layer model, all sites	Average bias, 23-layer model, all sites	Average difference, 23-layer model, w/o 2 high-latitude sites	Average bias, 23-layer model, w/o 2 high-latitude sites	Observed standard deviation, all sites
125	108.6	83.7	−18.7 (5%)	10.6 (3%)	72.4	13.6 (3%)	137
200	79.5	44.9	−46.8 (23%)	−24.9 (12%)	37.9	−29.0 (14%)	74.2
300	15.1	28.9	5.8 (8%)	20.8 (28%)	21.3	12.5 (17%)	32.2
500	9.3	10.6	7.5 (16%)	5.3 (11%)	8.7	2.5 (5%)	11.4
950	9.3	6.9	7.7 (31%)	2.0 (8%)	6.8	1.5 (6%)	9.9

Comparisons are between the 23-layer model and the 16 recommended sites of Logan et al. (1999), having excluded the two sites with four months or less data. Average differences are from the month-by-month absolute value differences between the model and the sondes. Average biases are with no absolute value included. Values in parentheses are percent bias with respect to observed values at these levels. The sites are: Resolute, Edmonton, Hohenpeissenberg, Sapporo, Boulder, Wallops Island, Tateno, Kagoshima, Naha, Hilo, Natal, Samoa, Pretoria, Aspendale, Lauder, and Syowa.

ACPD
3, 3939–3989, 2003

Table 4. NO_x budget

Source/sink	Annual mean Tg N yr^{-1}
Fossil fuels	20.9
Soils	5.8
Biomass burning	5.8
Lightning	6.5
Aircraft	0.6
Stratosphere	−0.6
Chemistry	−36.8
Dry deposition	−2.2

ACPD

3, 3939–3989, 2003

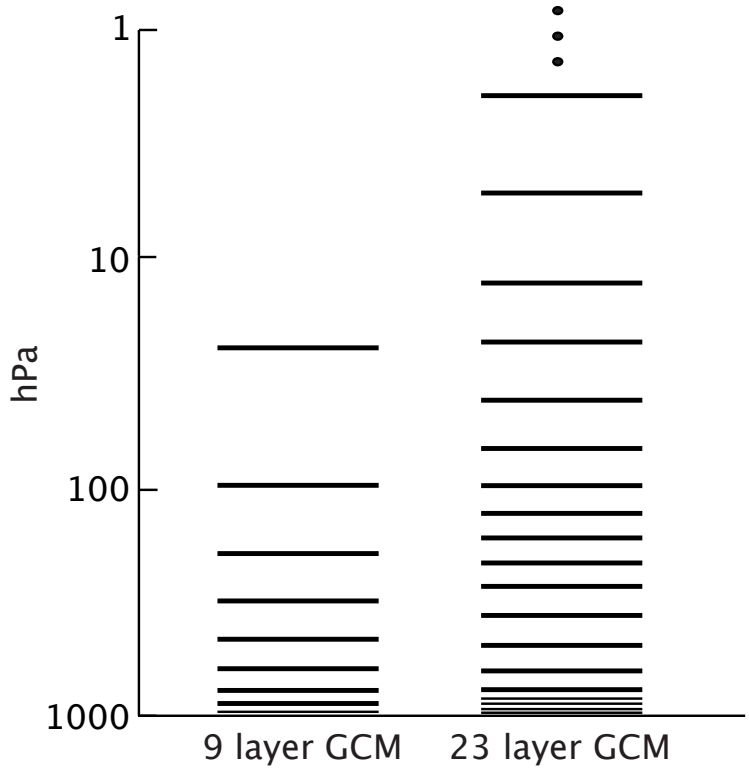

Fig. 1. Vertical layering in the older 9-layer model (layer centers at 959, 894, 786, 634, 468, 321, 201, 103, and 26.5 hPa) and in the new 23-layer model (layer centers at 972, 945, 907, 852, 765, 640, 498, 370, 280, 219, 171, 134, 102, 71.2, 43.9, 24.7, 13.9, 7.32, 3.05, 0.960, 0.303, 0.088, and 0.017 hPa). The four highest layers of the 23-layer model are not shown.

ACPD
3, 3939–3989, 2003

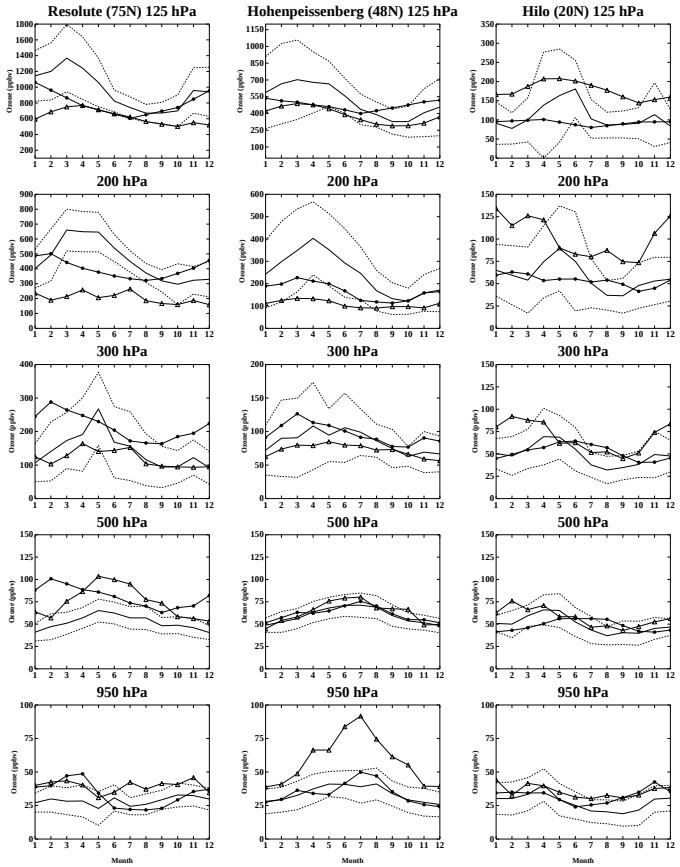

Fig. 2. Comparison of observed and simulated annual cycles of ozone at the indicated pressure levels and locations. Solid and dotted lines indicate ozonesonde measured mean values and standard deviations, respectively. Solid circles show mean values from the new model while open triangles show values from the older model. All values are mixing ratios in ppbv, and model values have been interpolated to the given sonde pressure levels.

ACPD
3, 3939–3989, 2003

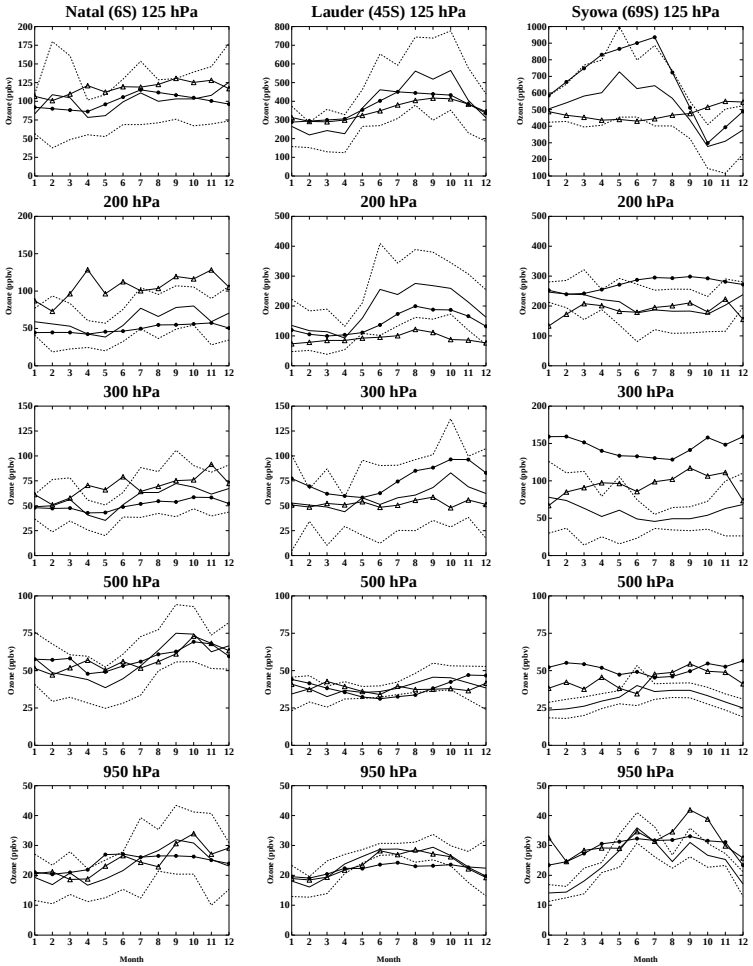

Fig. 2. Continued.

ACPD
3, 3939–3989, 2003

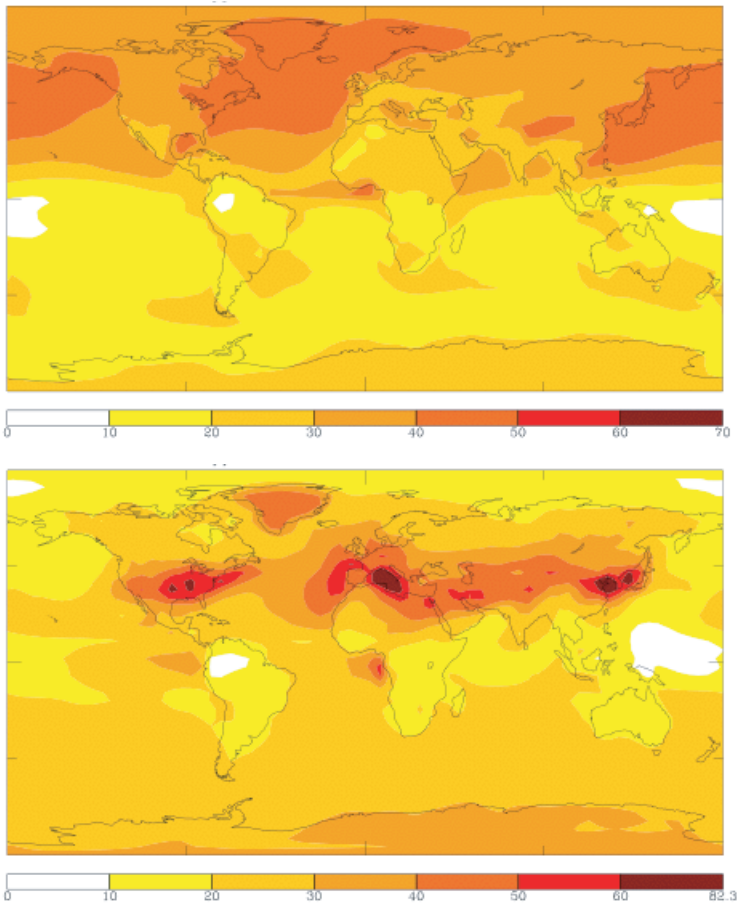

Fig. 3. Modeled ozone values (ppbv) in the lowest model layer for the present day. (top) January near-surface values, and (bottom) July values.

ACPD

3, 3939–3989, 2003

Preindustrial-to-present-day radiative forcing by tropospheric ozone

D. T. Shindell et al.

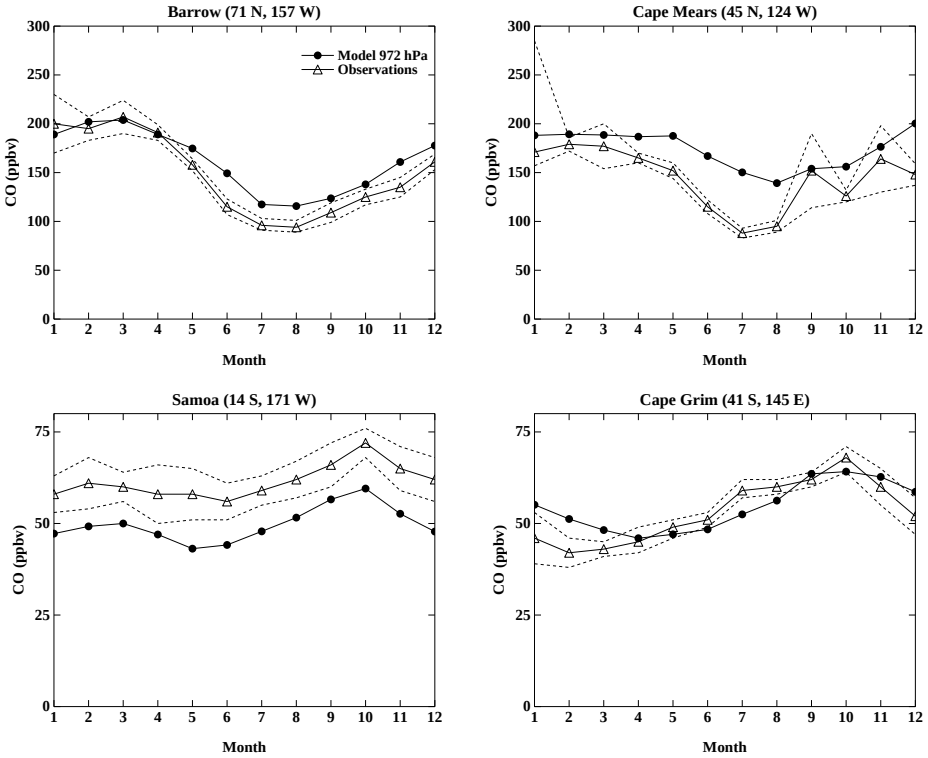

Fig. 4. Comparison of observed and simulated carbon monoxide near the surface. Open triangles and dotted lines indicate measured mean values and standard deviations, respectively. Solid circles show modeled mean values at the 972-hPa level.

ACPD
3, 3939–3989, 2003

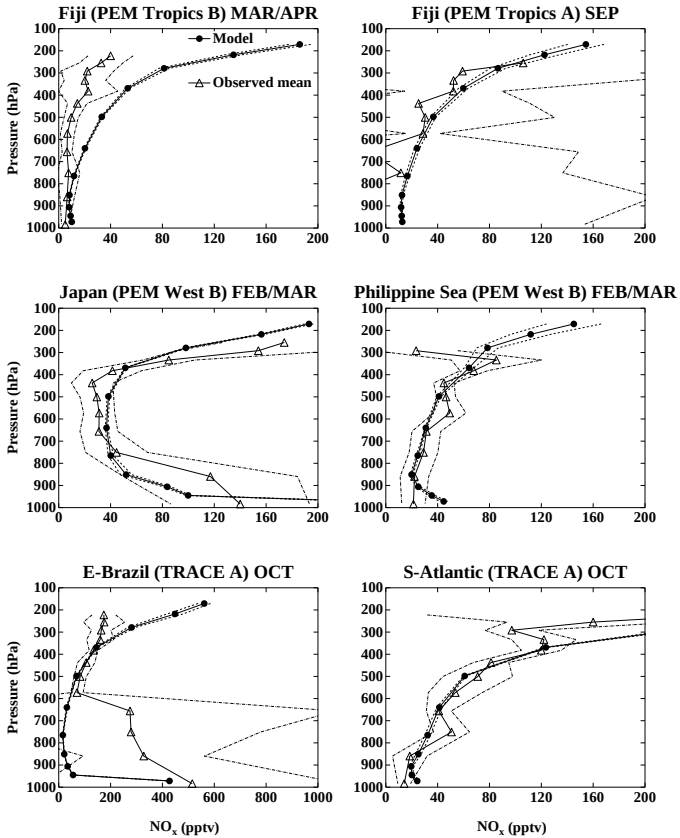

Fig. 5. Observed and simulated profiles of nitrogen oxides and nitric acid for various locations and seasons. Open triangles and dot-dash lines indicate measured mean values and standard deviations, respectively. Solid circles and dashed lines show modeled mean values and standard deviations. Observations are taken from Emmons et al. (2000).

ACPD
3, 3939–3989, 2003

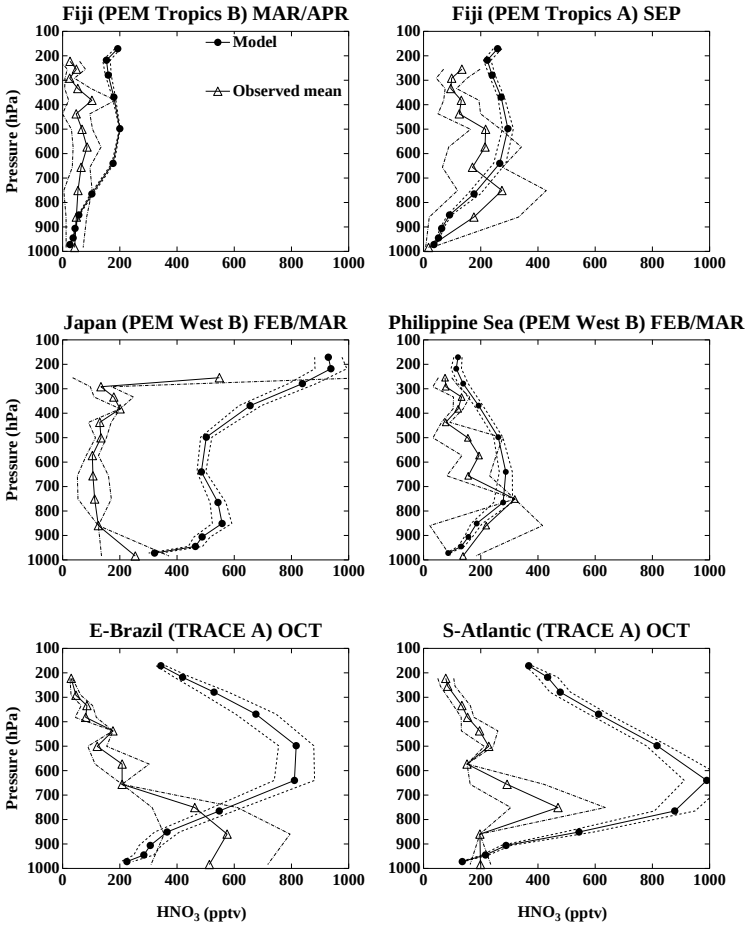

Fig. 5. Continued.

ACPD
3, 3939–3989, 2003

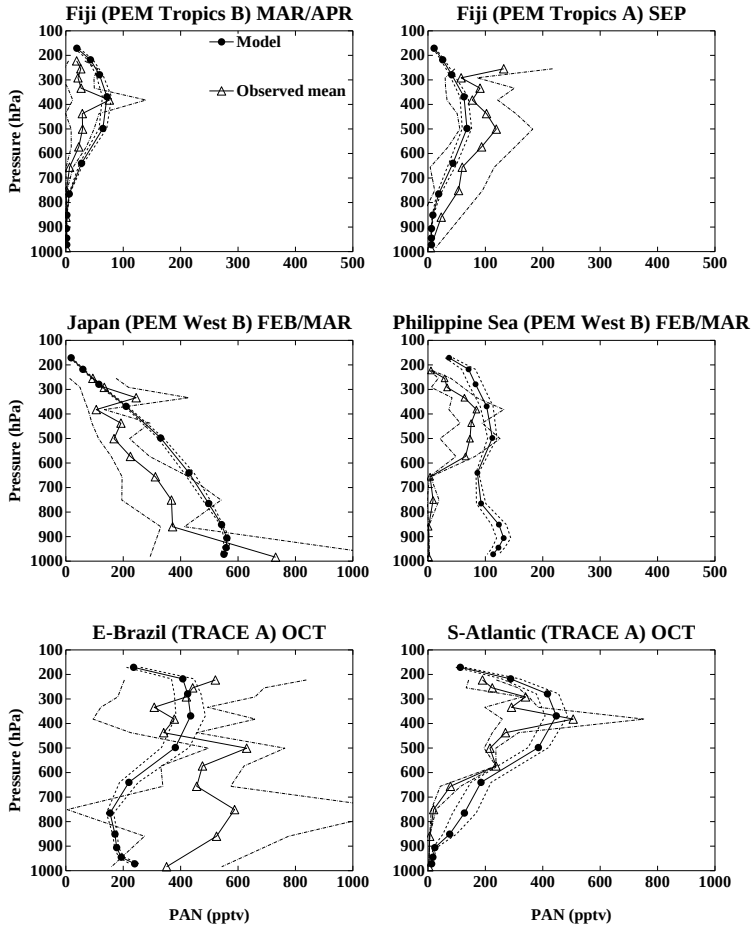

Fig. 6. Observed and simulated profiles of PANs for locations and seasons as in Fig. 5.

ACPD
3, 3939–3989, 2003

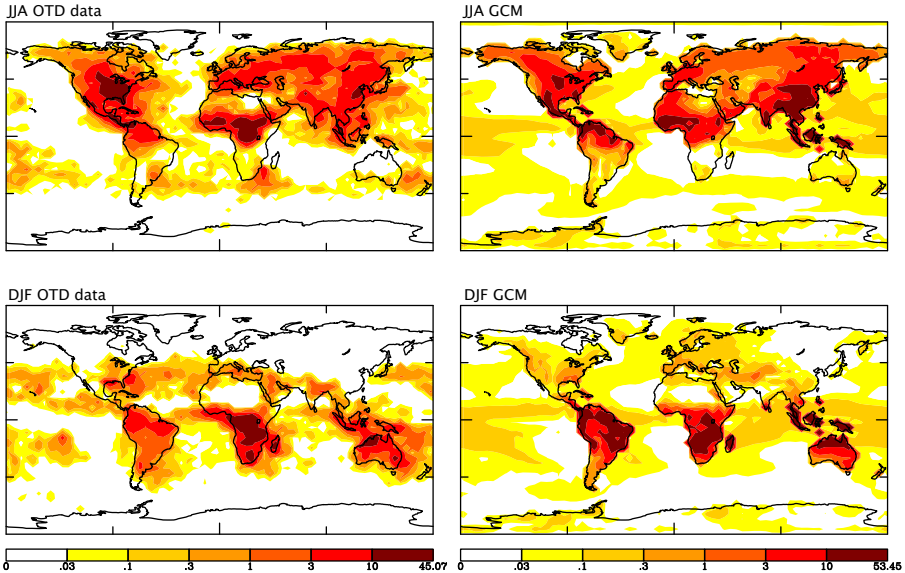

Fig. 7. Observed and simulated distributions of lightning flash rates (flashes/km^2/season). The left column shows observations from the Optical Transient Detector satellite during 1995–1996 (other years look similar), while the right shows model results. The top row is June–August, while the bottom is December-February. Note that there are no satellite observations at high latitudes.

ACPD
3, 3939–3989, 2003

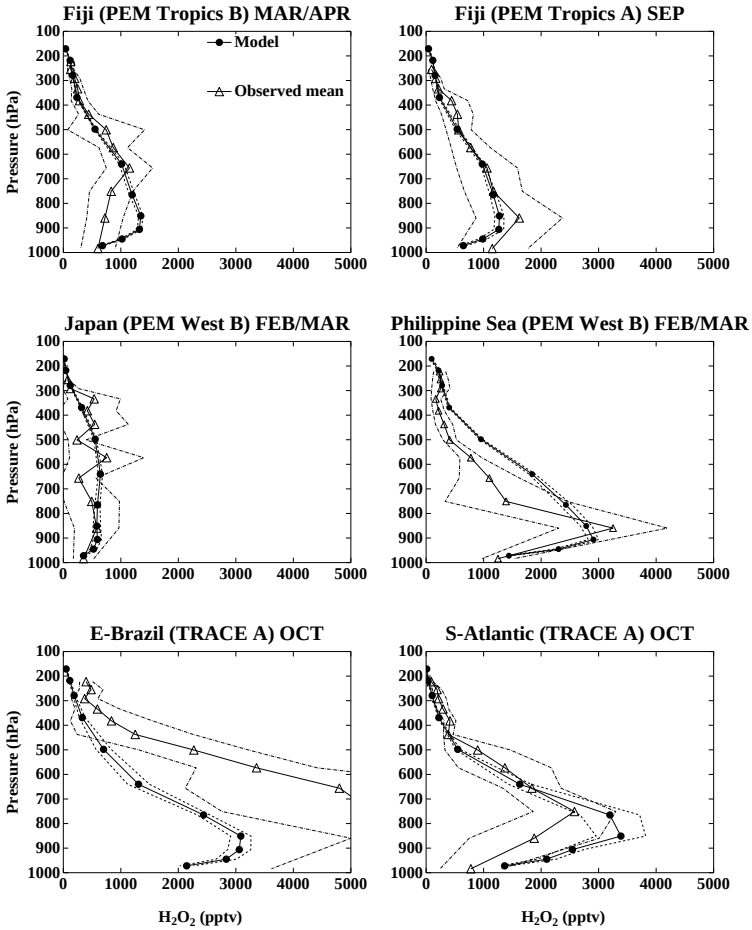

Fig. 8. Observed and simulated profiles of hydrogen peroxide for locations and seasons as in Fig. 5.

ACPD
3, 3939–3989, 2003

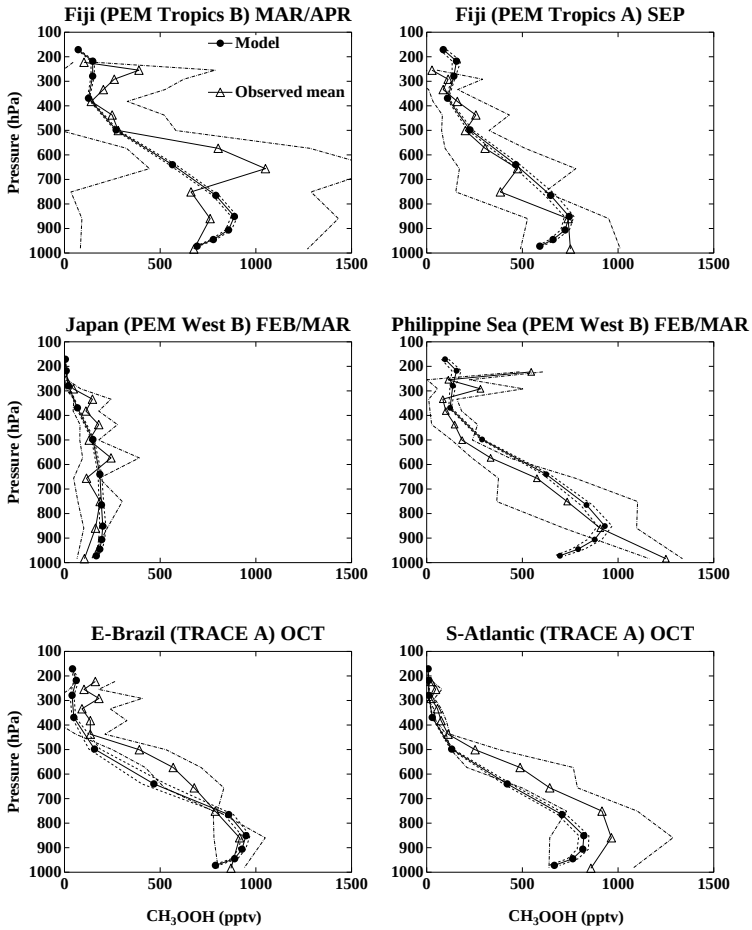

Fig. 9. Observed and simulated profiles of CH_3OOH for locations and seasons as in Fig. 5.

ACPD
3, 3939–3989, 2003

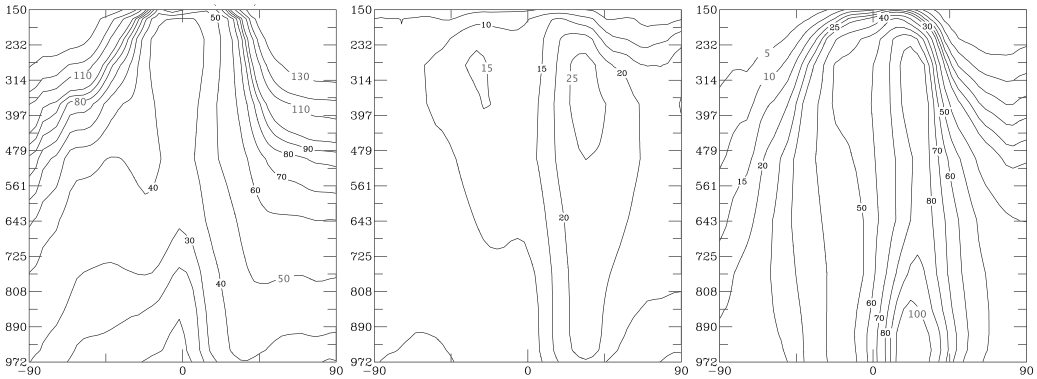

Fig. 10. Zonal mean ozone and ozone changes in the model. (Left) Zonal mean present-day ozone mixing ratios (ppbv). (Middle) The change from preindustrial to the present in mixing ratio (ppbv). (Right) The same change from preindustrial to the present in percent relative to the preindustrial amounts.

ACPD
3, 3939–3989, 2003

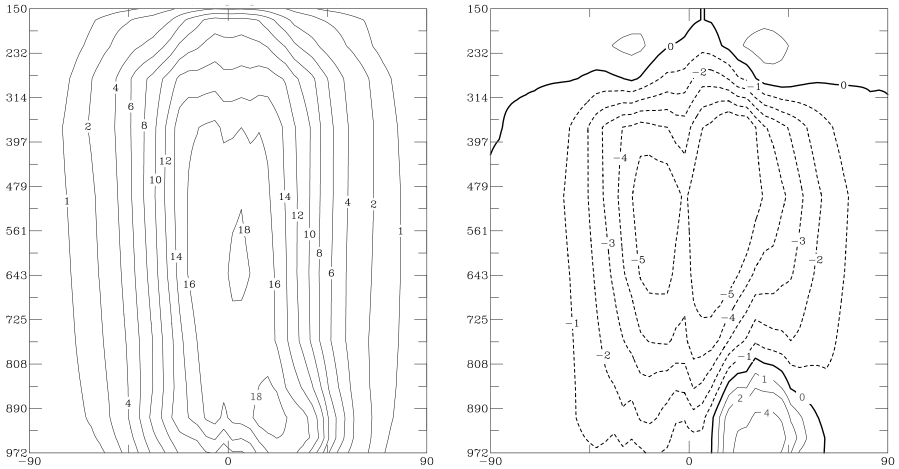

Fig. 11. (Left) Zonal mean hydroxyl in the present-day simulation, and (Right) zonal mean hydroxyl change from the preindustrial to the present. Both panels give values in units of 10^5 molecules cm^{-3}.

ACPD
3, 3939–3989, 2003

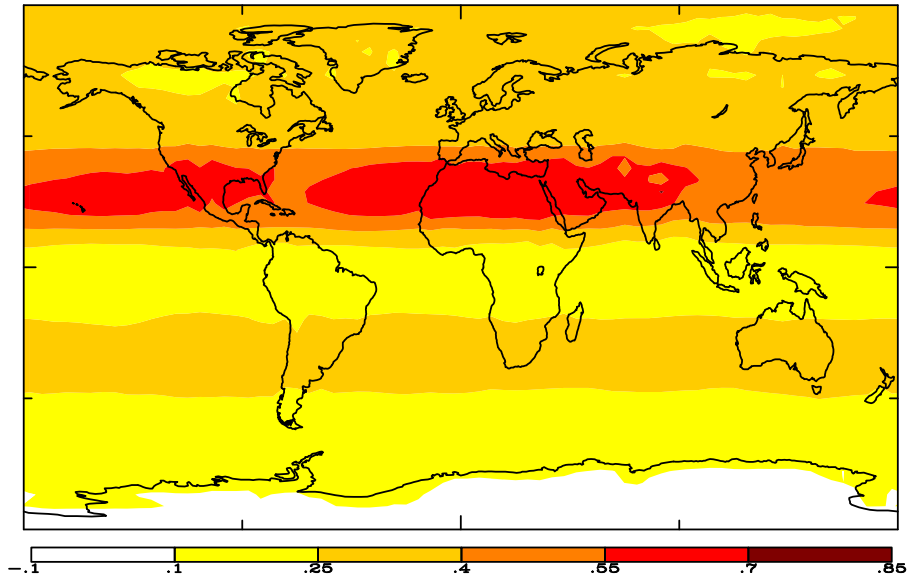

Fig. 12. Global mean annual average radiative forcing at the tropopause from the tropospheric ozone increase between the preindustrial and the present-day (W/m^2).

ACPD

3, 3939–3989, 2003

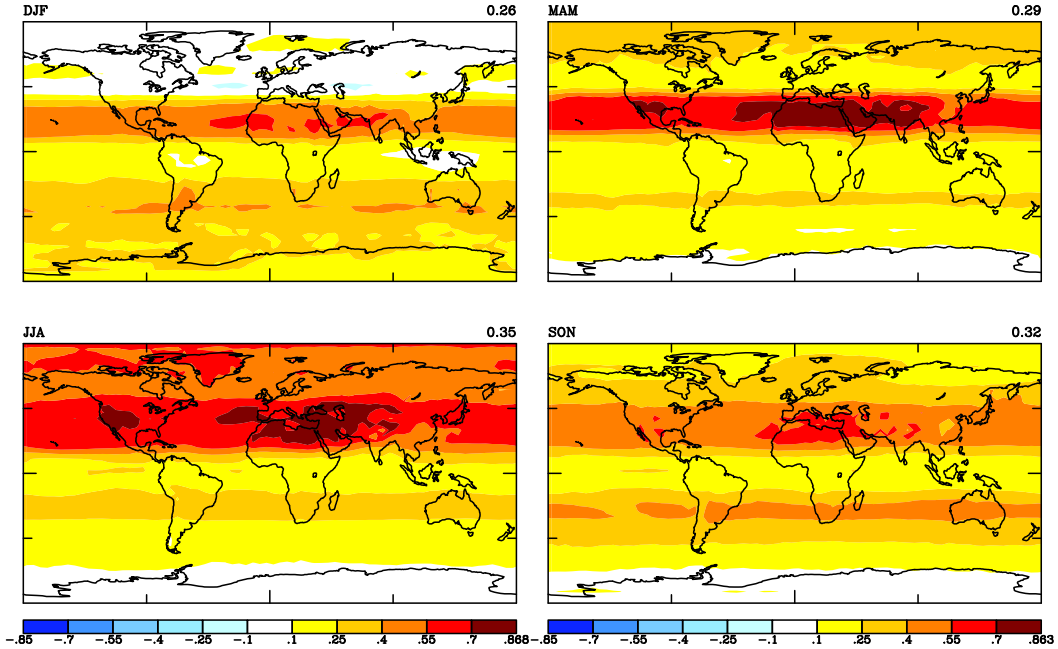

Fig. 13. Seasonally averaged radiative forcing at the tropopause from the tropospheric ozone increase between the preindustrial and the present-day (W/m^2). Global mean values are shown in the upper right corner of each plot.

ACPD
3, 3939–3989, 2003

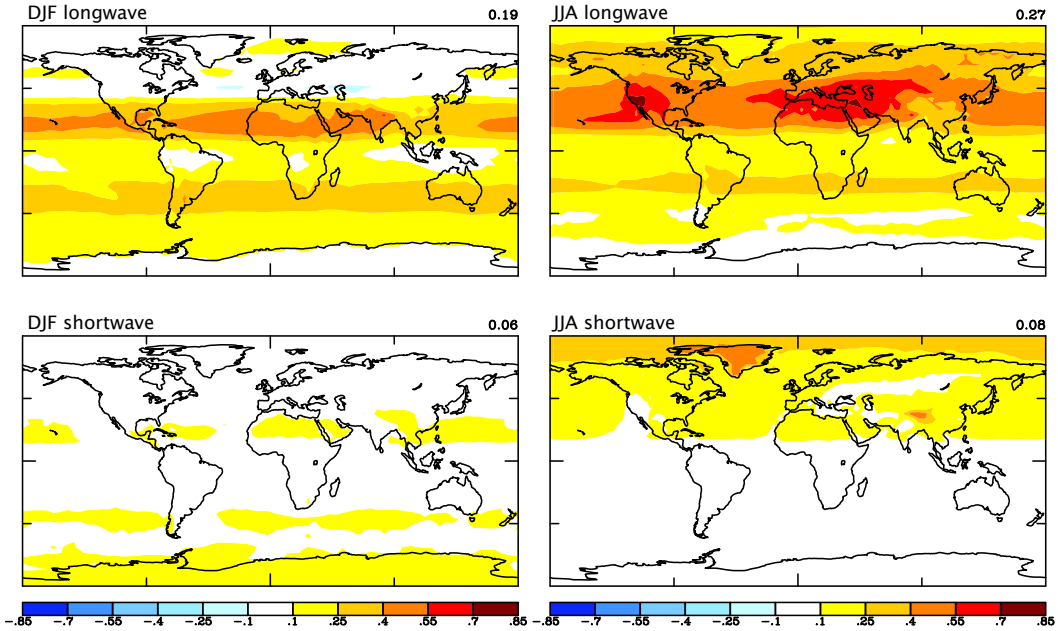

Fig. 14. Summer and winter shortwave and longwave radiative forcing at the tropopause from the tropospheric ozone increase between the preindustrial and the present-day (W/m^2). Global mean values are shown in the upper right corner of each plot.

ACPD
3, 3939–3989, 2003

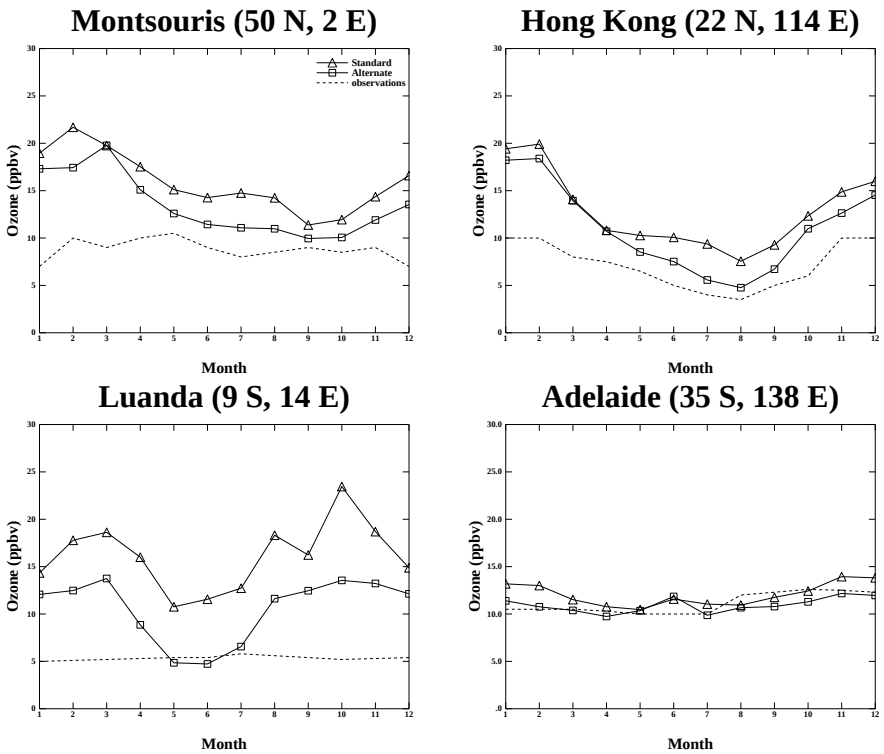

Fig. 15. Comparison between simulated preindustrial surface ozone levels and purported observations at the indicated locations (ppbv).

ACPD
3, 3939–3989, 2003